A Highly Selective Supramolecule Array Membrane Made of Zero-Dimensional Molecules for Gas Separation

Meng Zhao[+], Yujie Ban[+], Kun Yang, Yingwu Zhou, Na Cao, Yuecheng Wang, and Weishen Yang*

Abstract: *We orderly assembled zero-dimensional 2-methyl-imidazole (mim) molecules into unprecedented supramolecule array membranes (SAMs) through solvent-free vapor process-ing, realizing the intermolecular spacing of mim at ca. 0.30 nm available as size-sieving channels for distinguishing the tiny difference between H_2 (kinetic diameter: 0.289 nm) and CO_2 (kinetic diameter: 0.33 nm). The highly oriented and dense membranes yield a separation factor above 3600 for equimolar H_2/CO_2 mixtures, which is one order of magnitude higher than those of the state-of-the-art membranes defining 2017's upper bound for H_2/CO_2 separation. These SAMs define a new benchmark for molecular sieve membranes and are of para-mount importance to precombustion carbon capture. Given the range of supramolecules, we anticipate SAMs with variable intermolecular channels could be applied in diversified sepa-rations that are prevalent in chemical processes.*

Introduction

Intrinsically porous crystals, such as zeolites[1–3] and metal–organic frameworks (MOFs),[4–8] have been made into classical molecular sieve membranes for chemical separa-tions; their nanopores uphold selective transport and molec-ular discrimination. Previous studies have focused on the assembly of such membranes by means of three-dimensional microparticles[9–11] or two-dimensional nanosheets[12–16] as primary building blocks. However, the weak connections by nature between the neighboring "bricks" usually result in

intercrystalline gaps in membranes, which is catastrophic for molecular selectivity of separations.

Supramolecule assembly can be used to organize simple molecular precursors into an ever-increasing number of elegant structures through weak interactions (e.g. hydrogen bonding, donor-acceptor, π–π and van der Waals interactions, etc.).[17–19] Assemblies such as protein folding or lipid bilayers in nature[20,21] are gaining prominence because of their fascinating biological properties and highly ordered and complex entities. Separation membranes assembled from such programmed molecular-level building blocks are bound to be at the frontier of architecture design. These assemblies, if precise control of transport pathways for specific gas molecules is achieved, have been anticipated to define a new benchmark for molecular sieve membranes.

A representative supramolecule shows 2-methylimidazole (mim) in the $P2_12_12_1$ space group.[22] Two neighboring molecules engage in N−H⋯N hydrogen bonding interactions, leading to infinite chains. Such arrangements set no cavity, but rather a distance of ca. 0.30 nm shown in the typical (110) crystal face between adjacent chains (Supporting Informa-tion, Figure S1). In-situ infrared sorption measurements record a retention of CO_2 on mim crystal powder (Figure S2). The characteristic vibration peaks at 2338 cm^{-1} and 2359 cm^{-1} ascribing to R branch and P branch of the asymmetric stretching mode of CO_2, respectively, maintained stable on mim crystals after continuous N_2 sweeping for 90 min. It indicates the preference of mim for CO_2 (having a large quadrupole moment) over other gas molecules.[23] Never-theless, the preliminary sorption experiment (Figure S3) indicates that the sorbent bed of nonporous mim fails to realize a classical separation of H_2 with a smaller kinetic diameter (0.289 nm) from CO_2 (0.33 nm), whether through a size-sieving or a chemical sorption mechanism. It is impossible to envisage a breakthrough of mim for gas separations other than through ordered assembly of mim into membranes, in which the intermolecular spacings (ca. 0.30 nm) well-constrained by weak interactions would be available as channel-like molecular transport pathways.

As a proof-of-concept, we proposed supramolecule array membranes (SAMs) with mim as the molecular building blocks. However, it remains a challenge to induce site-specific nucleation of mim and to promote templated assembly of such organic molecules into ordered membranes. With this challenge in mind, we noted that metal–organic frameworks (MOFs) with open metal sites favor a binding of organic molecules, for example, organic molecules with N atoms,[24–26] through metal-donor bonds, and the abundance of active metal sites surrounding external MOF surface underpins the coordinative linkage of polymers,[27,28] bio-molecules[29] and

[*] M. Zhao,[+] Dr. Y. Ban,[+] K. Yang, Y. Zhou, N. Cao, Y. Wang,
Prof. Dr. W. Yang
State Key Laboratory of Catalysis, Dalian Institute of Chemical
Physics, Chinese Academy of Sciences
457 Zhongshan Road, Dalian 116023 (P. R. China)
and
University of Chinese Academy of Sciences
19A Yuquan Road, Beijing 100049 (P. R. China)
E-mail: yangws@dicp.ac.cn

Dr. Y. Ban[+]
Dalian National Laboratory for Clean Energy
457 Zhongshan Road, Dalian 116023 (P. R. China)

[+] These authors contributed equally to this work.

growth modulators[30] on MOFs to achieve surface coating, functionality ligation and definite core–shell structures. Inspired by these early manipulations on MOFs with open metal sites, we employed a facile vapor-sublimation-crystallization (VSC) process[31] to assemble mim SAMs on such layers of MOFs. Here, $Zn_2(dobdc)$ (where dobdc = 2,5-dioxido-1,4-benzenedicarboxylate; named MOF-74 or CPO-27) is designated, since it features one-dimensional pores (ca. 1.1 nm width) lined with coordinatively unsaturated Zn^{2+} sites that can readily anchor mim in vapor for supramolecule nucleation and recrystallization (Figure S4). We outline the scientific discoveries and breakthrough as follows: (i) Supramolecule mim were orderly assembled into membranes on MOF-74 grain layers. (ii) The oriented alignment of (110) crystal planes of mim renders its intermolecular spacing (ca. 0.30 nm) as a channel-like transportation pathway for H_2 and CO_2. (iii) The membranes show H_2/CO_2 selectivity above 3600, far beyond selectivities of the state-of-the-art membranes.

Results and Discussion

MOF-74 crystals were first produced by reaction of H_4dobdc with $Zn(NO_3)_2 \cdot 6H_2O$ in mixed solvents,[32] as demonstrated in Figure S5. The particle size, measured by dynamic light scattering (DLS), was 290 ± 200 nm (Figure S6). The thermogravimetry (TG) curve depicts a desolvation process of MOF-74 under thermal treatment (Figure S7). Accordingly, an obvious shift of Zn^{2+} peaks in X-ray photoelectron spectroscopy (XPS) analysis reveals that the open metal sites are gradually exposed with an increase of treatment temperature, together with a relaxation of Zn^{2+} coordination environment from a square bipyramidal conformation to a square pyramidal geometry (Figure 1a).

To assist mim assembly into SAMs, MOF-74 nanocrystal powders were introduced into the stainless-steel net (SSN) substrates by hand-scrubbing, forming closely packed grain layers as confirmed by X-ray diffraction (XRD) patterns (Figure 1b) and scanning electron microscopy (SEM) images (Figure 1c). Prior to the SAM assembly, the correlation of vapor pressure of mim with temperature in a sealed autoclave was probed in situ through a coupled sensor system (Figure S8). A vapor pressure-steady-state appeared ranging from 130 to 150°C (Figure S9), along with the fusion of mim. Thus, a controlled VSC process was implemented in a sealed autoclave to expose the grain layer into mim vapor at 150°C for 6 h, followed by cooling naturally in an oven (apparatus shown in Figure S10). This process enables mim to recrystallize and be assembled into the SAM on the surface of the SSN substrate. XRD patterns of the SAM displayed typical mim peaks (Figure 1b). Compared with the random mim powder, the relative intensity of the (110) plane of the SAM improved significantly (up to ca. 1323), which suggests an oriented lattice array on the surface of the substrate. In contrast, an analogous assembly process implemented on the bare substrate results in no phase attributable to mim (Figure S11), offering evidence regarding the necessity of MOF grain layers for the mim SAMs. The XRD peaks belonging to the MOF-74

grain layer are absent (Figure 1b), which signifies a solid phase change of MOF crystals in mim vapor.[33] SEM images of the SAMs show that the large-area laminae attached firmly to stainless-steel wires were surprisingly retained even after vigorous exfoliation in the ultra-high vacuum (ca. 10^{-4}–10^{-5} Pa) of the SEM (Figure 1c, bottom left; Figure S12). We speculate that the laminae built from mim scaffolds serve as secondary building blocks and stack in an oriented manner for mim SAMs, giving rise to the ordered alignment of (110) planes as documented by XRD patterns (Figure 1b). SEM images confirm the disappearance of the MOF-74 grain layer, and show that particles tend to deposit on stainless-steel wires (Figure 1c, bottom right). The lack of detectable MOF phase in XRD patterns might be attributed to an ultrathin deposition layer on the wires. Energy-dispersive X-ray spectroscopy (EDS) analysis coupled with SEM shows pronounced zinc content at the region near stainless-steel wires (Figure 1d), implying the specific accumulation of Zn-bearing particles. This finding raises the question of whether the deposition at the SAM/substrate interface is associated with a new MOF phase derived from MOF-74.

To answer this question and gain insight into the formation process of mim SAMs, the structural evolution starting from MOF-74 grain layers was traced by XRD (Figure 2a–f). To simulate the membrane assembly process, SSN supported MOF-74 grain layers were exposed to mim vapor with a temperature ramp rate of 2°C min^{-1}. A sudden cooling treatment along with the immediate removal of the vapor source upon reaching the target temperature (stage 1, Figure 2a) creates conditions unsuitable for mim condensation. The XRD pattern (Figure 2d) presents peaks alone belonging to the MOF-74 grain layer, and no apparent change is observed on its surface (Figure S13). Holding at 150°C for 2 h (stage 2, Figure 2a) encourages mim to invade the domain of the MOF-74 grain layer, concomitant with the structural evolution of MOF-74 (Figure 2d). We ascribe new XRD peaks to $Zn(mim)_2 \cdot (mim)_{0.5}$ crystals, also named zeolitic imidazolate framework-L (ZIF-L, Figure S14). ZIF-L here is derived from the reaction of MOF-74 and mim in this stage and presents a layer of squama-like grains on the SSN substrate (Figure S13). A synergistic process that includes holding at target temperature (for 2 and 4 h) and natural annealing (stage 3 and 4, Figure 2b) can also drive the MOF-74 conversion to ZIF-L (Figure 2e), evidenced by the presence of the white sediment on the surface of the substrate (Figure S13). Simultaneously, ZIF-L evolves into small grains, and tends to gather around the wires of the substrate instead of filling the voids (Figure S13). Prolonging holding time (typically for 6 h) contributes to mim peaks becoming dominant in XRD patterns (Figure 2c and f). A massive deposition of mim appears on the surface of the SSN substrate, corresponding to SAMs that are perfectly assembled. Nevertheless, ZIF-L transforms further into smaller particles intergrown on the wires (Figure S13), leading to a non-detectable signal in XRD patterns.

In light of the above analysis, we propose the assembly process and the microstructural model of the mim SAM, as shown in Figure 2g–i. Priority was given to mim molecules in the vapor to anchor at the open metal sites of closely packed
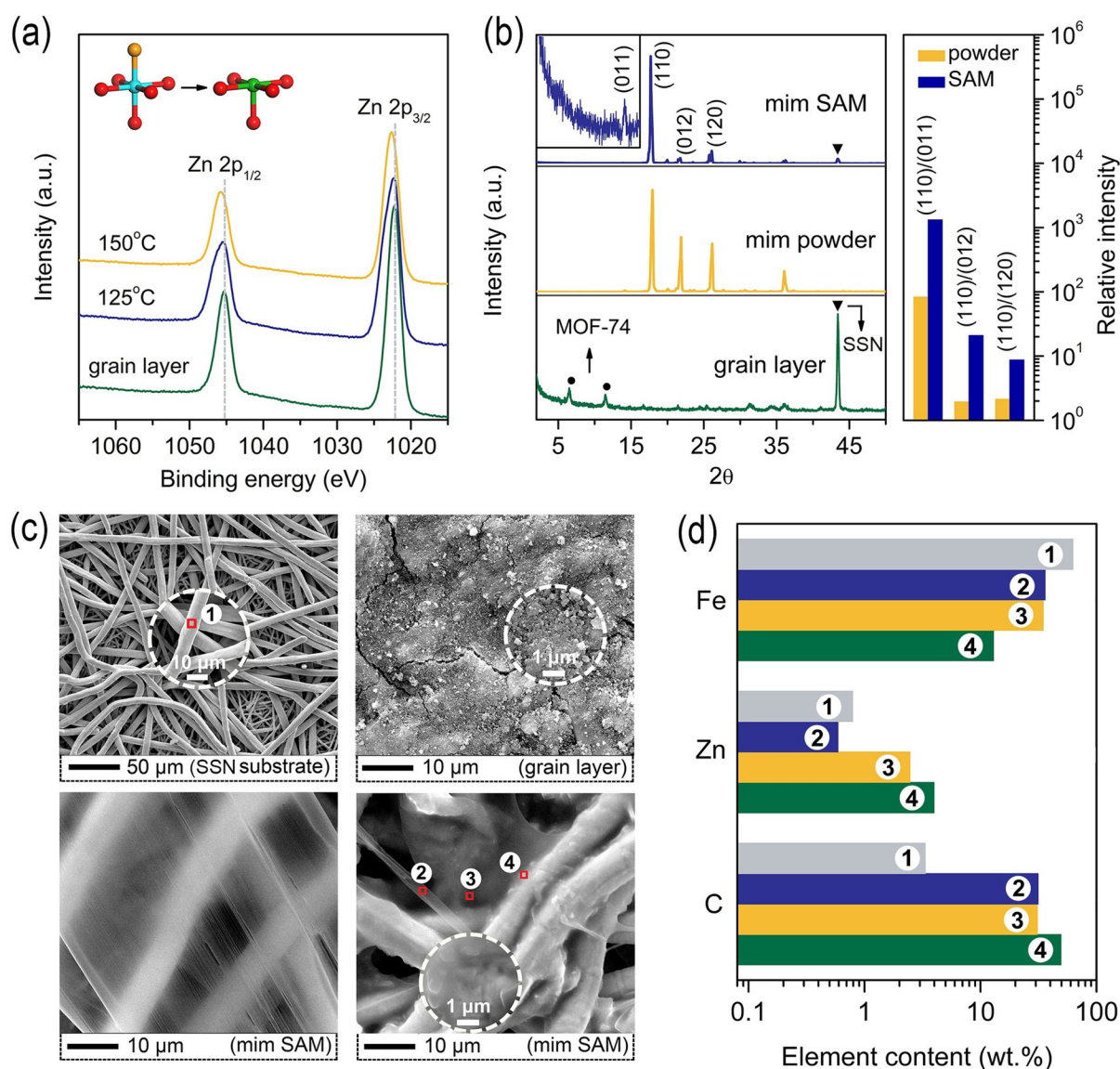
Figure 1. The ordered assembly of the mim SAM on the surface of the MOF-74 grain layer supported by the SSN substrate. a) XPS spectra of Zn^{2+} of the MOF-74 crystal powder under thermal treatment at different temperatures. b) XRD analysis of the oriented mim SAM relative to the random powder: patterns and relative intensity of crystal planes. Each pattern is scaled to a self-adaptive intensity axis for the visibility of weak diffraction peaks. Inset: magnified views of XRD patterns of the mim SAM in 2θ range of 2–16°. c) SEM images of the SSN substrate, MOF-74 grain layer and mim SAMs. Inset: magnified views at the inset point enclosed with dash circles. d) The element content of the selected area (marked with red squares) in (c) determined by EDS analysis.

MOF-74 particles through metal-donor (Zn-N) interactions (Figure 2g), producing high-density mim crystal nuclei simultaneously on the substrate. It is pivotal for the subsequent mim recrystallization and supramolecule propagation. Then, the pre-organized mim molecules, through N−H···N hydrogen bonding, are linked into oligomeric chains that are further assembled into the lattice array with orientation for SAMs (Figure 2i). Consequently, zigzag channels form between the adjacent mim chains, with roughly 0.30 nm width exactly falling between the kinetic diameters, for example, of H_2 and CO_2. A clear size-sieving effect can be anticipated in mim SAMs for H_2/CO_2 separation that is gaining prominence in precombustion carbon capture. It is noteworthy that, in mim assembly process, the coordination bonds of Zn-N, stronger

than those of Zn-O,[34] necessitate a total linker exchange of MOF-74 in the dense mim vapor, leading to the generation of ZIF-L particles with two-dimensional (2D) layered structure,[35] as shown in Figure 2h. We also tentatively study the potential of ZIF-L grain layers for mim assembly. An analogous vapor processing was implemented on ZIF-L grain layers (synthesized ex-situ, and transformed in situ from MOF-74 grain layers, see details in Supporting Information). The failure proves the necessity of MOF-74 grain layers for the early accumulation of high-density crystal nuclei that drive the assembly of mim into dense membranes in essence (Figure S15 and S16).

White light interferometry (WLI) as a surface-sensitive and non-destructive technique was also used to map the
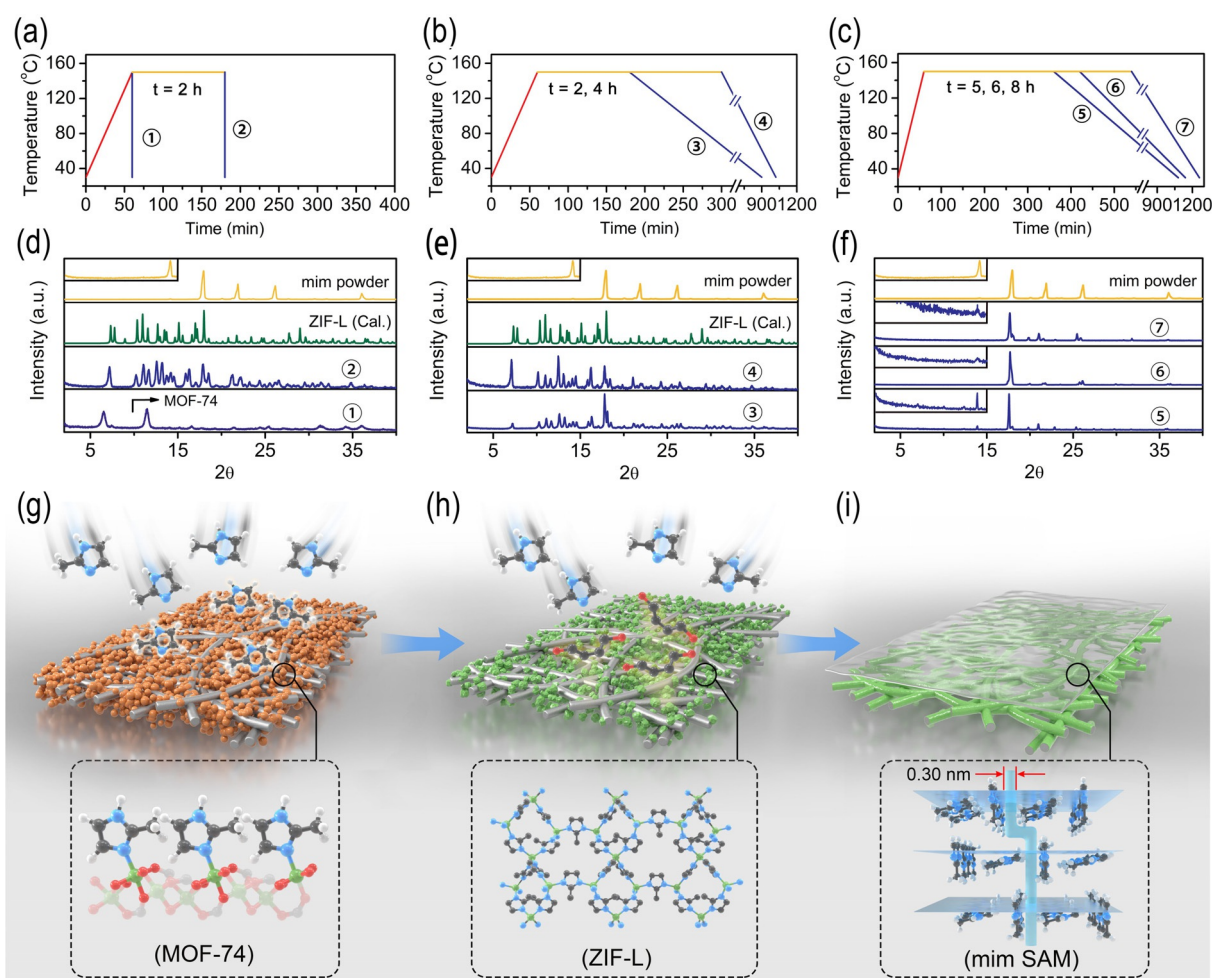
Figure 2. The structural evolution of the MOF-74 grain layer and the formation process of the mim SAM. a)–c) Dynamic temperature-time curves recorded in the home-made sealed autoclave. d)–f) XRD patterns of products collected at different stages in (a)–(c). Each pattern is scaled to a self-adaptive intensity axis for the visibility of weak diffraction peaks. Inset: magnified views of XRD patterns of corresponding products in 2θ range of 2–15°. g)–i) Illustration of the MOF-74 conversion to ZIF-L during the VSC and the microstructure model of the mim SAM. Zn-N interactions drive mim in vapor to land on the domain of the MOF-74 grain layer (g), along with the MOF-74 conversion to ZIF-L (h). MOF-74 and ZIF-L are modelled by particles of different morphology for discrimination, nonequivalent to their real features. Mim molecules are ultimately assembled into the SAM, concomitant with ZIF-L intergrown on the wires of the substrate (i). The channel-like molecular transport pathways (0.30 nm width) stem from the oriented alignment of (110) crystal planes on the surface of the substrate. In bottom dash panels, green, red, blue, dark grey and white balls represent Zn, O, N, C and H atoms, respectively; some H atoms are omitted for clarity. A portion of crystal structure, namely open Zn^{2+} nodes lining along c-axis, is shown for MOF-74, and a sheet unit cited from the layered structure is shown for ZIF-L for clarity.

surface of the mim SAM. Three-dimensional (3D) images reveal complete membrane layers filling voids in the SSN substrate, giving rise to a fairly even landscape (Figure 3a and b). Fourier transform infrared (FTIR) spectra feature asymmetric C=N vibrations (ν_{as}) of the mim SAM at 1676 cm^{-1} (Figure 3c). Infrared micrographs taken at this frequency provide spatially resolved chemical imaging of the SAM. The signal intensities are stable in the 2D scanning area (the absorbance difference lower than 1.3%), implying uniformity of the mim SAM at the millimeter area (Figure 3d).

Gas transported through mim SAMs (6-hour-assembly) was conducted with a continuous flow of H$_2$/CO$_2$ equimolar mixture using Wicke–Kallenbach method (Figure S17). The MOF-74 grain layers closely packed into the SSN substrates have an average H$_2$ permeance of 11780 GPU, and do not exhibit H$_2$/CO$_2$ separation selectivity (ca. 4.4 on average; lower than Knudsen selectivity, 4.7, determined by molecular

weight). The abrupt permeance drop of the mim SAM relative to the grain layer is indicative of the continuity and densification of the membrane. The time-dependent data collection illustrates a stable separation performance of the mim SAM during 270 hours of continuous testing (Figure 4a). An analysis of the gas permeation of mim SAMs shows that the 6-hour-assembly optimizes the H$_2$/CO$_2$ separation performance of the membrane because of its ideal continuity and densification, providing a H$_2$/CO$_2$ separation factor up to 3689 at ambient conditions (Figure 4b). The single-component gas permeation of the optimal mim SAM as a function of the kinetic diameter of gas molecules shows a clear cut-off between H$_2$ and CO$_2$, as well as H$_2$ and CH$_4$ (Figure 4c), attributable to an appropriate size-excluding behavior through intermolecular galleries (Figure 2i). In addition, we also notice that CH$_4$ has much higher permeance than CO$_2$, although CH$_4$ (kinetic diameter: 0.38 nm) is larger than CO$_2$
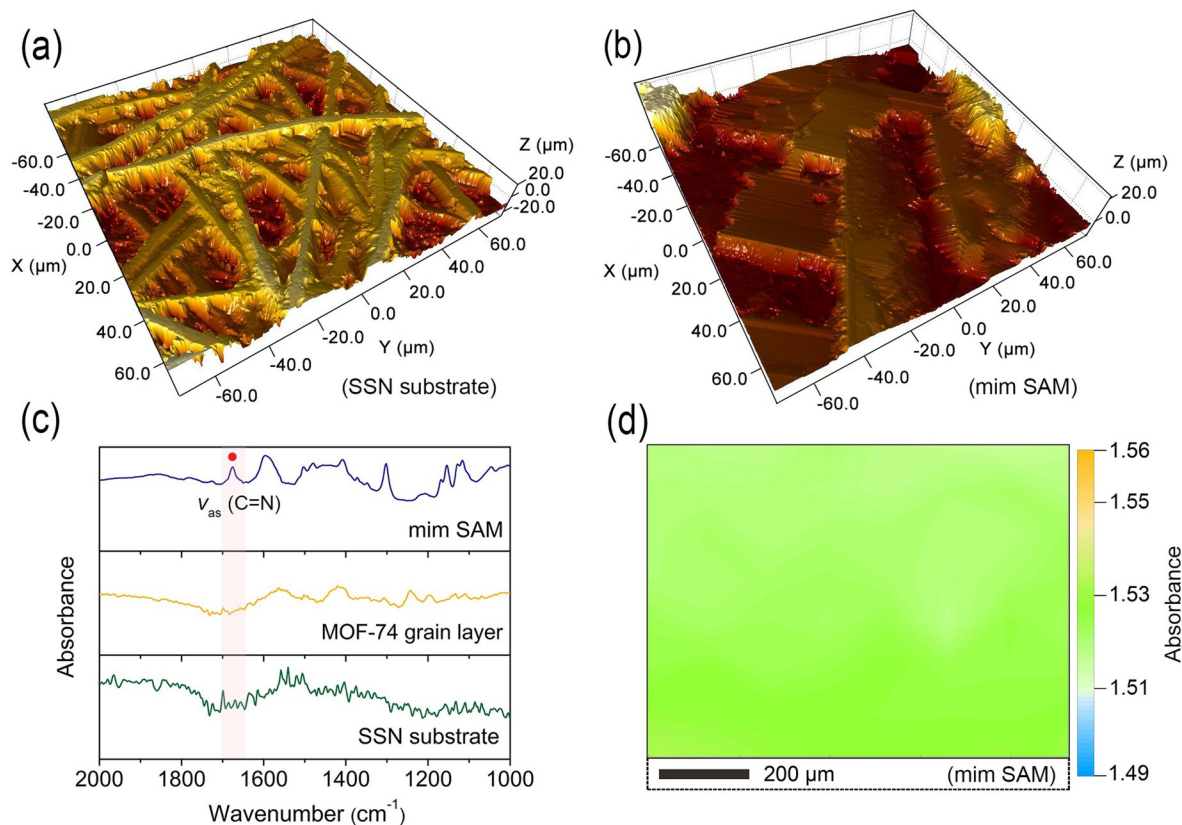
Figure 3. The surface morphology of the mim SAM probed by surface sensitive techniques with spatial resolution. a),b) 3D landscape of the SSN substrate (a) and mim SAM (b) using WLI technique. c),d) FTIR spectra of the mim SAM (c) and the 2D micrograph (d) using characteristic vibrations [ν_{as} (C=N)] in (c).

(kinetic diameter: 0.33 nm). In light of in situ infrared sorption measurements (Figure S2), we speculate that the affinity of CO_2 to mim leads to a detainment of CO_2 on the membrane surface (Figure S2) and a slow transport through channels, boosting the molecular sieving potential of the SAM dramatically between H_2 and CO_2. Furthermore, different from traditional molecular sieve membranes,[36] SAMs show a noticeable reversed CH_4 selectivity (far beyond Knudsen selectivity, 1.7 of CH_4/CO_2), whether in the case of single permeation or mixed gas separation (Figure 4c). The temperature-dependent adsorption experiments quantify the affinity of CO_2 to mim (Figure S18 and Table S1–S3). The near zero-coverage adsorption enthalpy of CO_2 on mim was -12.0 kJ mol^{-1}, corresponding to 16 and 3 times of that of H_2 (-0.762 kJ mol^{-1}) and CH_4 (-3.82 kJ mol^{-1}). To further illustrate the transport mechanism, single gas permeations at three different temperatures (298 K, 308 K and 318 K) were conducted. Temperature-dependent Arrhenius plots reveal that elevating temperature conduces to a remarkable increase of CO_2 permeance because of the weakened CO_2-mim affinity but has a very slight effect on H_2 and CH_4 permeances (Figure 5a). The activation energy of gas permeation through SAMs is 2.35 kJ mol^{-1} for H_2, 29.7 kJ mol^{-1} for CO_2 and 7.10 kJ mol^{-1} for CH_4. The activation energy of gas diffusion was determined from the activation energy of gas permeation minus the corresponding adsorption enthalpy. Clearly, as shown in Figure 5b, CO_2 diffusing through SAMs faces an exceptionally large energy barrier (41.7 kJ mol^{-1})

over H_2 (3.11 kJ mol^{-1}) and CH_4 (10.9 kJ mol^{-1}), which validates why the molecular sieving potential of the SAM is dramatically between H_2 and CO_2 and why the membrane prefers to transporting CH_4 rather than CO_2.

Furthermore, we made a comparison with literature. The separation properties of the mim SAMs far exceed the latest upper bound for H_2/CO_2 separation and are much higher than those of a wide range of membranes reported to date (Figure 4d), including 3D/2D zeolite membranes, 3D/2D MOF membranes, GO membranes (including composites), laminar C_3N_4/Mxene/LDH/ZrPP membranes, covalent organic framework (COF) membranes, polymer membranes, mixed-matrix membranes and carbon membranes.

Conclusion

We utilize MOF-74 with open metal nodes to induce site-specific nucleation of supramolecules and assemble well-known mim molecules into unprecedentedly oriented SAMs. Thanks to the ordered arrangement of mim crystal planes, the intermolecular spacings (spacings between adjacent hydrogen-bonded mim chains) that feature a width between the size of H_2 and CO_2 serve as the channel-like molecular transport pathways of membranes, demonstrating an impressive size-sieving behavior for this gas pair. The mim SAMs show H_2/CO_2 selectivities one order of magnitude higher than those of the state-of-the-art membranes that define 2017's upper
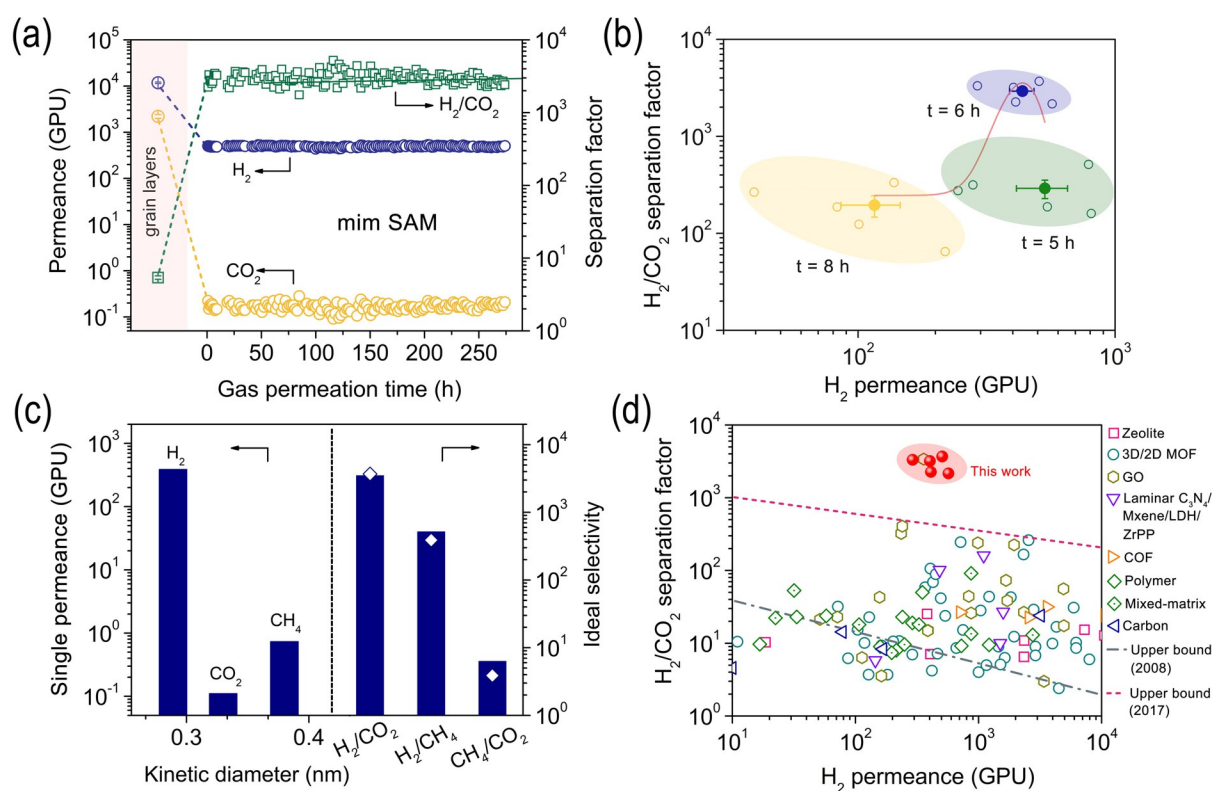
Figure 4. Gas permeation of mim SAMs with a feed pressure of 1 bar at room temperature. a) Equimolar binary H_2/CO_2 separation characteristics (permeances and separation factors) of the typical mim SAM (6-hour-assembly) as a function of gas permeation time. b) H_2/CO_2 separation factors versus H_2 permeances for equimolar binary H_2/CO_2 mixture through mim SAMs with assembly time of 5 h, 6 h, and 8 h. The average value with error bars (solid symbols) of permeances and separation factors of membranes were calculated from measurements of five independent membranes (open symbols). c) Single-component gas permeance through the optimal mim SAM (6-hour-assembly) and ideal selectivity determined by the ratios of single gas permeances. The rhombus symbols indicate the corresponding selectivity in mixed gas separations. d) Comparison of membranes in this work with a wide range of membranes reported to date (Table S4) for H_2/CO_2 separation in terms of separation factor versus H_2 permeance.
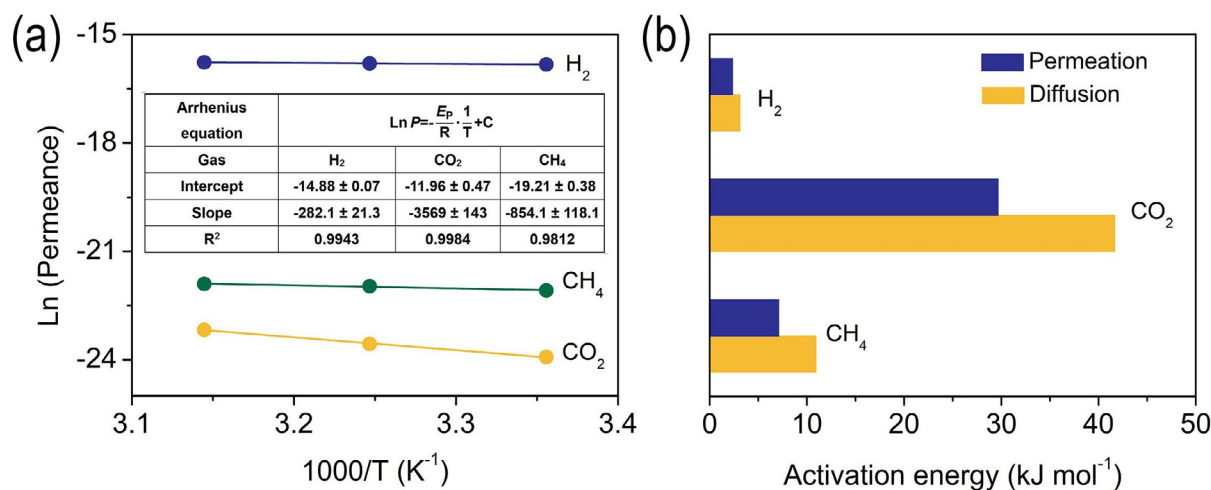
Figure 5. Transport mechanism of mim SAMs. a) Arrhenius plots of single-component permeances with a feed pressure of 1 bar. b) Activation energy of gases for permeation and diffusion.

bound for H_2/CO_2 separation. In SAMs, the zero-dimensional building blocks join together by term of supramolecule interactions, resulting in the absence of the intercrystalline gaps, which guarantees an effective mass-transfer through

intermolecular spacings instead of an undesirable leakage through non-selective gaps. Our success opens the door to the creation of a variety of SAMs with intermolecular galleries applicable to distinguish the subtle size/shape differences of

a pair of gas molecules. From the perspective of methodology, further efforts should be directed towards the scalable fabrication of high-quality "active" grain layers; this is a feasible way to achieve extreme homogeneous membranes. Another pivotal issue arises from the precise control of the propagation of supramolecules during temperature programmed vapor processing. Further work will enable a wide range of application of SAMs to energy-efficient chemical separation processes.

Acknowledgements

Conflict of Interest

The authors declare no conflict of interest.

[1] X. C. Xu, W. S. Yang, J. Liu, L. W. Lin, *Adv. Mater.* **2000**, *12*, 195–198.

[2] T. C. T. Pham, H. S. Kim, K. B. Yoon, *Science* **2011**, *334*, 1533–1538.

[3] M. A. Carreon, S. Li, J. L. Falconer, R. D. Noble, *J. Am. Chem. Soc.* **2008**, *130*, 5412–5413.

[4] A. Phan, C. J. Doonan, F. J. Uribe-Romo, C. B. Knobler, M. O'Keeffe, O. M. Yaghi, *Acc. Chem. Res.* **2010**, *43*, 58–67.

[5] K. Sumida, D. L. Rogow, J. A. Mason, T. M. McDonald, E. D. Bloch, Z. R. Herm, T.-H. Bae, J. R. Long, *Chem. Rev.* **2012**, *112*, 724–781.

[6] T. Kitao, Y. Zhang, S. Kitagawa, B. Wang, T. Uemura, *Chem. Soc. Rev.* **2017**, *46*, 3108–3133.

[7] A. Knebel, B. Geppert, K. Volgmann, D. I. Kolokolov, A. G. Stepanov, J. Twiefel, P. Heitjans, D. Volkmer, J. Caro, *Science* **2017**, *358*, 347–351.

[8] A. J. Brown, N. A. Brunelli, K. Eum, F. Rashidi, J. R. Johnson, W. J. Koros, C. W. Jones, S. Nair, *Science* **2014**, *345*, 72–75.

[9] H. Bux, F. Liang, Y. Li, J. Cravillon, M. Wiebcke, J. Caro, *J. Am. Chem. Soc.* **2009**, *131*, 16000–16001.

[10] Q. Hou, S. Zhou, Y. Wei, J. Caro, H. Wang, *J. Am. Chem. Soc.* **2020**, *142*, 9582–9586.

[11] X. Liu, N. K. Demir, Z. Wu, K. Li, *J. Am. Chem. Soc.* **2015**, *137*, 6999–7002.

[12] M. Y. Jeon, D. Kim, P. Kumar, P. S. Lee, N. Rangnekar, P. Bai, M. Shete, B. Elyassi, H. S. Lee, K. Narasimharao, S. N. Basahel, S. Al-Thabaiti, W. Xu, H. J. Cho, E. O. Fetisov, R. Thyagarajan, R. F. DeJaco, W. Fan, K. A. Mkhoyan, J. I. Siepmann, M. Tsapatsis, *Nature* **2017**, *543*, 690–694.

[13] Y. Peng, Y. Li, Y. Ban, H. Jin, W. Jiao, X. Liu, W. Yang, *Science* **2014**, *346*, 1356–1359.

[14] M. Dakhchoune, L. F. Villalobos, R. Semino, L. Liu, M. Rezaei, P. Schouwink, C. E. Avalos, P. Baade, V. Wood, Y. Han, M. Ceriotti, K. V. Agrawal, *Nat. Mater.* **2020**, *19*, https://doi.org/10.1038/s41563-41020-00822-41562.

[15] X. R. Wang, C. L. Chi, K. Zhang, Y. H. Qian, K. M. Gupta, Z. X. Kang, J. W. Jiang, D. Zhao, *Nat. Commun.* **2017**, *8*, 14460.

[16] Y. Sun, Y. Liu, J. Caro, X. Guo, C. Song, Y. Liu, *Angew. Chem. Int. Ed.* **2018**, *57*, 16088–16093; *Angew. Chem.* **2018**, *130*, 16320–16325.

[17] R. Chakrabarty, P. S. Mukherjee, P. J. Stang, *Chem. Rev.* **2011**, *111*, 6810–6918.

[18] T. Yokoyama, S. Yokoyama, T. Kamikado, Y. Okuno, S. Mashiko, *Nature* **2001**, *413*, 619–621.

[19] J. A. Theobald, N. S. Oxtoby, M. A. Phillips, N. R. Champness, P. H. Beton, *Nature* **2003**, *424*, 1029–1031.

[20] G. Kiss, N. Çelebi-Ölçüm, R. Moretti, D. Baker, K. N. Houk, *Angew. Chem. Int. Ed.* **2013**, *52*, 5700–5725; *Angew. Chem.* **2013**, *125*, 5810–5836.

[21] T. Kunitake, *Angew. Chem. Int. Ed. Engl.* **1992**, *31*, 709–726; *Angew. Chem.* **1992**, *104*, 692–710.

[22] B. Hachuła, M. Nowak, J. Kusz, *J. Chem. Crystallogr.* **2010**, *40*, 201–206.

[23] S. Evjen, A. Fiksdahl, H. K. Knuutila, *Ind. Eng. Chem. Res.* **2019**, *58*, 10533–10539.

[24] T. M. McDonald, J. A. Mason, X. Kong, E. D. Bloch, D. Gygi, A. Dani, V. Crocellà, F. Giordanino, S. O. Odoh, W. S. Drisdell, B. Vlaisavljevich, A. L. Dzubak, R. Poloni, S. K. Schnell, N. Planas, K. Lee, T. Pascal, L. F. Wan, D. Prendergast, J. B. Neaton, B. Smit, J. B. Kortright, L. Gagliardi, S. Bordiga, J. A. Reimer, J. R. Long, *Nature* **2015**, *519*, 303–308.

[25] X. Zhao, X. Bu, Q.-G. Zhai, H. Tran, P. Feng, *J. Am. Chem. Soc.* **2015**, *137*, 1396–1399.

[26] F.-M. Zhang, L.-Z. Dong, J.-S. Qin, W. Guan, J. Liu, S.-L. Li, M. Lu, Y.-Q. Lan, Z.-M. Su, H.-C. Zhou, *J. Am. Chem. Soc.* **2017**, *139*, 6183–6189.

[27] C. Li, J. Liu, K. Zhang, S. Zhang, Y. Lee, T. Li, *Angew. Chem. Int. Ed.* **2021**, *60*, 14138–14145; *Angew. Chem.* **2021**, *133*, 14257–14264.

[28] B. Yi, Y.-L. Wong, C. Hou, J. Zhang, Z. Xu, X. Yao, *Adv. Mater. Interfaces* **2021**, *8*, 2001202.

[29] W. Zhu, G. Xiang, J. Shang, J. Guo, B. Motevalli, P. Durfee, J. O. Agola, E. N. Coker, C. J. Brinker, *Adv. Funct. Mater.* **2018**, *28*, 1705274.

[30] S. Hermes, T. Witte, T. Hikov, D. Zacher, S. Bahnmüller, G. Langstein, K. Huber, R. A. Fischer, *J. Am. Chem. Soc.* **2007**, *129*, 5324–5325.

[31] X. Ye, Y. Liu, Q. Han, C. Ge, S. Cui, L. Zhang, X. Zheng, G. Liu, J. Liu, D. Liu, X. Tao, *Chem. Mater.* **2018**, *30*, 412–420.

[32] J. E. Bachman, Z. P. Smith, T. Li, T. Xu, J. R. Long, *Nat. Mater.* **2016**, *15*, 845–849.

[33] W. Wu, J. Su, M. Jia, Z. Li, G. Liu, W. Li, *Sci. Adv.* **2020**, *6*, eaax7270.

[34] D. Yu, Q. Shao, Q. Song, J. Cui, Y. Zhang, B. Wu, L. Ge, Y. Wang, Y. Zhang, Y. Qin, R. Vajtai, P. M. Ajayan, H. Wang, T. Xu, Y. Wu, *Nat. Commun.* **2020**, *11*, 927.

[35] Z.-X. Low, J. Yao, Q. Liu, M. He, Z. Wang, A. K. Suresh, J. Bellare, H. Wang, *Cryst. Growth Des.* **2014**, *14*, 6589–6598.

[36] Y. Jeong, S. Hong, E. Jang, E. Kim, H. Baik, N. Choi, A. C. K. Yip, J. Choi, *Angew. Chem. Int. Ed.* **2019**, *58*, 18654–18662; *Angew. Chem.* **2019**, *131*, 18827–18835.